1

1   Title: **Dual brain cortical calcium imaging reveals social interaction-**

2   **specific correlated activity in mice.**

3   Abbreviated title: Imaging inter-mouse brain synchronization

4   Nicholas J. Michelson[1,2,] Federico Bolaños[1,2], Luis A. Bolaños[1,2], Matilde Balbi[1,2], Jeffrey M.

5   LeDue[1,2], and Timothy H. Murphy[1,2,*]

6   1 Department of Psychiatry, Kinsmen Laboratory of Neurological Research;
7   2 Djavad Mowafaghian Centre for Brain Health, University of British Columbia,
8   Vancouver, British Columbia, Canada, V6T 1Z3;
9

10 Contributions: F.B., L.B., M.B., N.J.M., and T.H.M. performed animal experiments. F.B., T.H.M.,

11 N.J.M. and J.M.L. wrote the paper. F.B., L.B., J.M.L., and T.H.M. developed the hardware and

12 software for the apparatus. F.B., N.J.M., and J.M.L wrote the analysis. L.B., F.B., N.J.M., and

13 J.M.L drew models and figures.

14 *Correspondence to: Timothy H Murphy thmurphy@mail.ubc.ca

15 Number of figures: 5

16 Tables 1

17 1 video

18

19

29

30

31 **Abstract**

32 We employ cortical mesoscale calcium-imaging to observe brain activity in two head-fixed mice

33 in a staged social touch-like interaction. Using a rail system, mice are brought together to a

34 distance where macrovibrissae of each mouse make contact. Cortical signals were recorded

35 from both mice simultaneously before, during, and after the social contact period. When the

36 mice were together, we observed bouts of mutual whisking and cross-mouse correlated cortical

37 activity in the vibrissae cortex. This correlated activity was specific to individual interactions as

38 the correlations fell in trial-shuffled mouse pairs. Whisk-related global GCAMP6s signals were

39 greater in cagemate pairs during the together period. The effects of social interaction extend

40 outside of regions associated with mutual touch and had global synchronizing effects on cortical

41 activity. We present an open-source platform to investigate the neurobiology of social

42 interaction by including mechanical drawings, protocols, and software necessary for others to

43 extend this work.

44

45

46 **Keywords:** mouse, cortex, social interaction, GCAMP, mesoscale, whisker

47

48

49   **Introduction**

50   The power of social interaction and touch is undisputed across the animal kingdom. In

51   many animals, the presence of a conspecific partner may elicit competitive behavior,

52   reproductive arousal, fear, or other attention-demanding states. Traversal of a social interaction

53   requires each subject to dynamically integrate its internal state and previous experiences with

54   the behavior of its partner and other environmental variables (P. Chen & Hong, 2018).

55   Simultaneously recording neural activity from two individuals engaged in social interaction

56   (Montague et al., 2002) revealed that interacting humans exhibit correlated neural activity

57   (Funane et al., 2011; Liu et al., 2017). Interestingly, this emergent property seems to convey

58   information regarding the context or development of the interaction (Dikker et al., 2017; Jiang et

59   al., 2015; Yang, Zhang, Ni, De Dreu, & Ma, 2020).

60   Later experiments in mice and bats observed inter-animal neural synchronization at

61   cellular and circuit-level scales, using optical and electrical recording methodologies (Kingsbury

62   et al., 2019; Zhang & Yartsev, 2019). In the mouse prelimbic cortex, single neurons were shown

63   to encode specific self-initiated and partner-initiated competitive social behaviors; and the

64   degree of synchronization between neuronal network activity in each animal was correlated with

65   rank differences in the social dominance hierarchy (Kingsbury et al., 2020). Other studies have

66   shown that prelimbic cortex activity directly modulates social dominance status (Wang et al.,

67   2011; Zhou et al., 2017).

68   Many circuits throughout the brain shape different aspects of social behavior (Dölen,

69   Darvishzadeh, Huang, & Malenka, 2013; Gunaydin et al., 2014; B. Guo et al., 2019; Rogers-Carter

70   et al., 2018; Sych, Chernysheva, Sumanovski, & Helmchen, n.d.; Tschida et al., 2019; Walsh et al.,

71   2018; Zhou et al., 2017). Given the complex motivational and decision-making states involved

72   with social interaction, it follows that the neural representation of social information may be

73   widespread and distributed throughout the brain similar to other phenomena (Allen et al., 2019,

74   2017; Pinto et al., 2019; Steinmetz, Zatka-Haas, Carandini, & Harris, 2019). For example, in

75   rodents, information regarding the sex of a conspecific partner is represented in many areas

76   (Ebbesen, Bobrov, Rao, & Brecht, 2019), including prelimbic cortex (Kingsbury et al., 2020),

77   whisker somatosensory cortex (Bobrov, Wolfe, Rao, & Brecht, 2014), and medial amygdala (Li et

78   al., 2017). Moreover, basic sensory signaling is modulated during a social context (Cohen,

79   Rothschild, & Mizrahi, 2011; Lenschow & Brecht, 2015).

80   Investigation of the macro-scale organization of neural dynamics during social interaction

81   therefore represents an important step forward in understanding the social brain. Widefield

82   cortical calcium imaging provides an opportunity to observe neural activity across the entire

83   dorsal cortex *in vivo* (Clancy, Orsolic, & Mrsic-Flogel, 2019; Gilad & Helmchen, 2020; Musall,

84   Kaufman, Juavinett, Gluf, & Churchland, 2019; Pinto et al., 2019; Vanni, Chan, Balbi, Silasi, &

85   Murphy, 2017; Xiao et al., 2017), but its application to social neuroscience is largely unexplored

86   (MacDowell & Buschman, 2020). In this work, we present a paradigm where multi-subject cortical

87   functional GCaMP imaging is employed during staged interactions between mice. We also

88   provide detailed resources to help investigators set up inexpensive mesoscale cortical GCaMP

89   imaging rigs suitable for dual mouse brain imaging. We find that face to face interactions

90   between mice synchronize cortical activity over wide-scales and this phenomenon is not limited

91   to regions primarily processing whisker/touch dependent signals.

92

93 **Methods**

94 *Animals and experimental considerations*

95 All procedures were approved by the University of British Columbia Animal Care

96 Committee and conformed to the Canadian Council on Animal Care and Use guidelines and

97 reported according to the ARRIVE guidelines. Transgenic GCaMP6s tetO-GCaMP6s x CAMK tTA

98 (Wekselblatt, Flister, Piscopo, & Niell, 2016) were obtained from the Jackson Laboratory. All mice

99 used in this study were males >60 days of age and housed in social housing (n=15 mice up to 4

100 mice/cage from 6 cages) with 12-h light/12-h dark cycles and free access to food and water. We

101 did not employ female mice or male and female mouse pairs because of potential for variation

102 across the estrous cycle that may alter social behavior.

103 *Surgical procedure*

104 Chronic windows were implanted on male mice that were at least 8 weeks old, as

105 previously described in (Silasi, Xiao, Vanni, Chen, & Murphy, 2016). Fur and skin were removed

106 from the dorsal area of the head, exposing the skull over the entire two dorsal brain hemispheres.

107 After cleaning the skull with a phosphate buffered saline solution, a titanium head-fixing bar was

108 glued to the skull above lambda (Figure 1a) and reinforced with clear dental cement (Metabond).

109 A custom cut coverslip was glued with dental cement on top of the skull (Figure 1a), with the

110 edges of the window reinforced with a thicker mix of dental cement similar to the procedure of

111 (Silasi et al., 2016). Mice recovered for at least seven days prior to imaging or head-fixation.

112 *Social Dominance Measurements*

113   Social rank was estimated using the tube-test assay (Fan et al., 2019). Briefly, mice were

114   introduced to either end of a narrow plexiglass tube (32cm long, 2.5cm inner diameter). Upon

115   meeting in the middle, mice compete by pushing each other to get to the opposite side. The

116   mouse which pushes the other back out of the tube is deemed the winner. All combinations of

117   mice within a cage were tested in a round robin format to determine the linear dominance

118   hierarchy. Tube test tournaments were repeated weekly to assess stability of the hierarchy.

119   *Social Interaction Experiments*

120   Two Raspberry Pi imaging rigs were set up facing each other, and initially separated by 14

121   cm. A parts list and assembly instructions for the Raspberry Pi widefield imaging rig are included

122   in the supplementary information. One imaging rig was placed atop a translatable rail (Sherline

123   5411 XY Milling Machine Base), which was driven by a stepper motor to bring the mouse

124   (hereafter referred to as the moving mouse) into the proximity of the other mouse (stationary

125   mouse, 6-12 mm inter-snout distance) (see Table 1 and supplemental build guide for details).

126   Thus, we imaged dorsal cortical activity from two head-restrained mice simultaneously, while

127   varying the distance between snouts (Figure 1b-c, Supplemental Video 1). Mice were habituated

128   to the system for at least one week prior to conducting experiments by head-fixing the animals

129   each day and performing all procedures (e.g. translation, imaging) without the presence of the

130   other mouse.

131   The entire imaging system was housed inside a box lined with acoustic foam, thereby

132   reducing ambient light and noise. Throughout the experiment, audio recordings were obtained

133   at 200 kHz using an ultrasonic microphone (Dodotronic, Ultramic UM200K) positioned within the

134   recording chamber approximately 5cm from each mouse's snout. Audio recordings were

135   analyzed for ultrasonic vocalizations using the MATLAB toolbox DeepSqueak (Coffey, Marx, &

136   Neumaier, 2019).

137
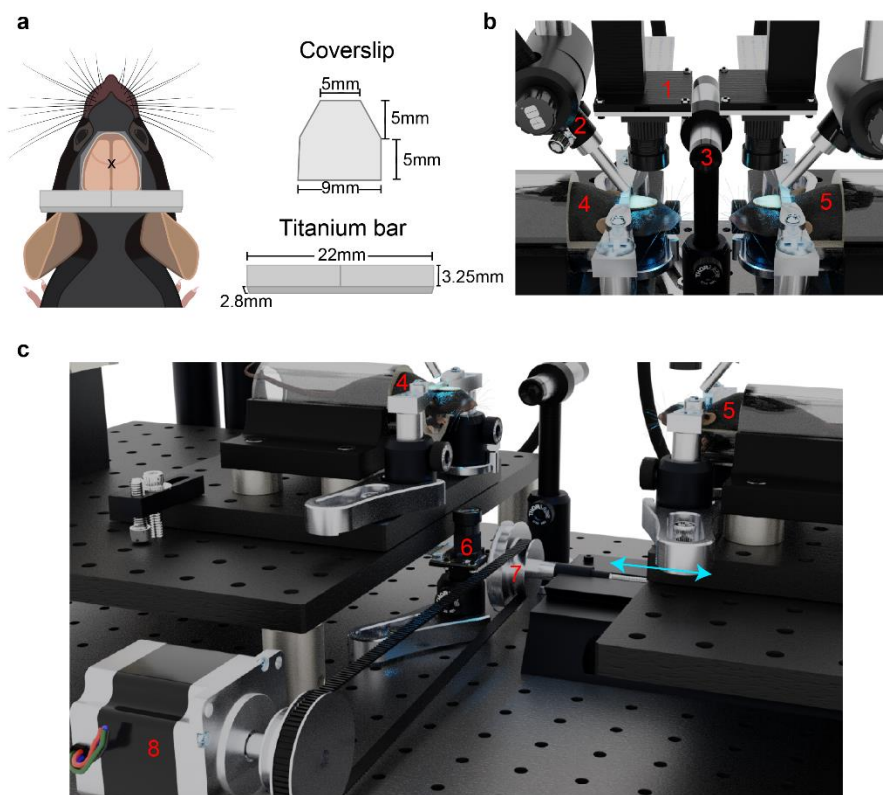
Figure 1. Setup for dual mouse brain imaging system. A) Cartoon depiction of surgical preparation for transcranial mesoscale imaging, with custom cut coverslip and titanium bar for head fixation. B) Close-up view of mouse positioning during the interaction phase of the experiment. C) Larger field of view render of the imaging system. Numbered components are as follows: 1) Raspberry Pi brain imaging camera; 2) GCaMP excitation and hemodynamic reflectance LED light guide; 3) ultrasonic microphone; 4) stationary mouse; 5) moving mouse; 6) Raspberry Pi infrared behavior camera; 7) stage translation knob; 8) stepper motor with belt controlling stage translation. Blue arrows indicate direction of motion of the translatable rail.

146

147   *Behavior Imaging*

148 The experimental setup was illuminated with an infrared (850 nm) light emitting diode

149 (LED) and behaviors were monitored using an infrared Raspberry Pi camera (OmniVision, OV5647

150 CMOS sensor). Behavior videos were captured at a framerate of 90 frames per second (fps) with

151 a resolution of 320x180 pixels. The camera was positioned such that the stationary mouse was

152 always included in the field of view and both mice were clearly visible when they were together

153 (Figure 2a).

154

155 *GCaMP Image Acquisition*

156 GCaMP activity was imaged using Raspberry Pi Cameras (OmniVision OV5647 CMOS

157 sensor) equipped with a triple-bandpass filter (Chroma 69013m). The lens on the camera has a

158 focal length of 3.6mm with a field of view of ~10.2x10.2mm, leading to a pixel size of ~40 microns.

159 24-bit RGB images of GCaMP activity and reflectance were captured at ~30fps and 256x256

160 resolution. The three cameras (2 brain and 1 behavior) were configured such that one camera

161 was used to start the acquisition of the other two. Each cortex was illuminated using two LEDs

162 simultaneously, where one light source (short blue, 447.5 nm Royal Blue Luxeon Rebel LED SP-

163 01-V4 with Thorlabs FB 440-10 nm band pass filter) provides information about hemodynamic

164 changes during the experiment (Xiao et al., 2017), and the other light source (long blue, 470nm

165 Luxeon Rebel LED SP-01-B6 with Chroma 480/30 nm) excites GCaMP. The LEDs were turned on

166 and off using a transistor-transistor logic (TTL) output from an isolated pulse stimulator (AM-

167 Systems Model 2100) which was triggered immediately after the start of each experiment. This

168 sudden change in illumination was used during post-hoc analysis to synchronize frames across

169 cameras. With the current recording setup, the Raspberry Pi cameras occasionally drop frames

170   as a result of writing the data to the disk. We identified the location of dropped frames by tagging

171   each frame with a timestamp and found that consecutive frames were rarely dropped. Given the

172   small number of dropped frames, and the relatively slow kinetics of GCaMP6s (T.-W. Chen et al.,

173   2013), the lost data was estimated by interpolating the signal for each pixel, thus preserving the

174   temporal resolution.

175   *GCaMP Image Processing*

176   Image pre-processing was conducted with Python using a Jupyter Notebook (Kluyver et

177   al., 2016). Further analysis was conducted using MATLAB (MathWorks, Natick MA, USA). Green

178   and blue channels, which contain the GCaMP6s fluorescence and the blood volume reflectance

179   signals respectively (Ma et al., 2016; Valley et al., 2020; Wekselblatt et al., 2016), were converted

180   to $\Delta F/F_0$. The baseline image, estimated as the mean image across time for the entire recording,

181   was subtracted from each individual frame (ΔF). The result of this difference was then divided by

182   the mean image, yielding the fractional change in intensity for each pixel as a function of time

183   ($\Delta F/F_0$).

184   To correct for hemodynamic artifacts, blue light (440+/-5nm) reflectance $\Delta F/F_0$ was

185   subtracted from the green fluorescence $\Delta F/F_0$. In this way, small changes in the brain reflectance

186   due to blood volume changes do not influence the epifluorescence signal. While we acknowledge

187   that a green reflectance strobing and model-based correction may be advantageous (Ma et al.,

188   2016), certain technical aspects of the Raspberry Pi camera (which is needed to perform this

189   experiment due to its small form factor) such as its rolling shutter and inability to read its frame

190   exposure clock prevent this method from being implemented. The short blue wavelength

191   (440nm) is close to an oxy/deoxygenated hemoglobin isobestic point, and the reflected light

192   signal correlates well with the green reflectance signal (Xiao et al., 2017), suggesting that this

193   method effectively captures signal changes resulting from hemodynamic activity. Moreover,

194   hemodynamic changes are relatively small compared to the signal-noise-ratio of GCaMP6s (Dana

195   et al., 2014).

196   Occasionally, noisy extreme pixel values for ΔF/F0 were observed due to imaging near the

197   edge of the window or due to the ratio-metric calculation of the ΔF/F0. To reduce their

198   contribution, pixels exceeding a threshold value were set to be equal to the threshold, thereby

199   reducing artifacts from smoothing or filtering that might result from inclusion of aberrantly large

200   ΔF/F0 values. The threshold was set at the mean +/- 3.5x the standard deviation of each pixel's

201   time-series for GCaMP data, and at 15% ΔF/F0 for the reflectance data (which is larger than

202   expected reflectance signal values). The ΔF/F0 signal was then smoothed with a Gaussian image

203   filter (sigma=1) and filtered using a 4th order Butterworth bandpass filter (0.01-12.0Hz) (Vanni &

204   Murphy, 2014).

205   *Behavior Quantification*

206   To extract behavior events, a region of interest (ROI) was manually drawn on the behavior

207   video over each mouse's whiskers and forelimbs (Figure 2a). The motion energy within each ROI

208   was calculated by taking the absolute value of the temporal gradient of the mean pixel value

209   within the ROI. The resulting motion energy was smoothed via convolution with a Gaussian kernel

210   (σ=5 frames) and a threshold was established at the mean + 1 standard deviation to detect

211   behaviors. This analysis captured whisker and forelimb movements for the stationary mouse for

212   the entirety of the experiment, and for the moving mouse only during the interaction phase

213   (Figure 2c).

Inter-brain correlation analysis

215   Correlation across brains was calculated using the Pearson's correlation coefficient (PCC).

216   To compare correlations across trial phases, the inter-brain PCC was calculated for a one-minute

217   period during initial-separate, together, and final-separate trial phases. Global signals were

218   calculated as the median $\Delta F/F_0$ across the entire dorsal cortex, whereas individual regions were

219   selected from coordinates with respect to bregma according to the Allen Institute brain atlas, and

220   the corresponding time-series data was calculated as the mean activity within a 5x5 pixel area

221   surrounding each region location. Time-varying coherence between global signals was estimated

222   with multitaper methods over a 45 second window with 22.5 second overlap using the Matlab

223   Chronux toolbox with a time-bandwidth product of 5 and a taper number of 9 (Bokil, Andrews,

224   Kulkarni, Mehta, & Mitra, 2010; Mitra & Bokil, 2009).

Whisker triggered event analysis

226   Calcium activity surrounding whisk-initiation events (+/-1s) were extracted from each

227   whisk event and averaged across events per trial. Whisk events were excluded if any of the

228   following conditions were met: 1) they occurred coincidentally with forelimb movements, 2) they

229   occurred within 1 second of the previous whisk event, or 3) total duration exceeded 0.5 seconds.

230   Self-initiated whisking activity therefore refers to averaged calcium activity of mouse A

231   surrounding whisk events initiated by mouse A, whereas partner-initiated maps refer to averaged

232   calcium activity of mouse A surrounding whisk events initiated by mouse B.

233   *Statistics*

234   Statistical tests were conducted with MATLAB. All data were tested for normality using a

235   Kolmogorov-Smirnov test prior to subsequent statistical analyses. Correlation values were

236   transformed using Fisher's z-transformation. Comparisons between two groups were conducted

237   using two-tailed t-tests for parametric data and Wilcoxon signed rank tests for non-parametric

238   data. Comparisons between trial phases were assessed using a repeated measures ANOVA with

239   post-hoc Bonferroni correction for multiple comparisons. All statistically significant results were

240   observed on the GCaMP signals alone as well as the hemodynamic corrected signals.

241   *Resource Availability*

242   Resources to assist in building cortex-wide GCaMP imaging systems, including parts lists,

243   assembly instructions, and CAD files are available in the supplemental information and at the

244   Open Science Framework project entitled Dual Brain Imaging. Code for image acquisition,

245   preprocessing, and analysis are available at the University of British Columbia's Dynamic Brain

246   Circuits   in   Health   and   Disease   research   cluster's   GitHub

247   (https://github.com/ubcbraincircuits/dual-mouse). Data are available in the Federated Research

248   Data Repository at https://doi.org/10.20383/101.0303.

249   **Results**

250   *Mice Exhibit Correlated Bouts of Behavior During Social Interaction*

251   Forelimb and whisker movements were monitored for each mouse to measure behavior

252   (Figure 2A) using a camera positioned underneath the interacting mice (Figure 1C). The stationary

253   mouse's behavior was captured throughout the entire experiment, while the moving mouse's

254   behavior acquisition was limited to the social interaction period only (Figure 2B). . Bouts of

255   forelimb and whisker movements often occur simultaneously (Figure 2C), and the amount of time

256   spent actively moving whiskers or forelimbs, expressed as percentage of time spent behaving in

257   each trial phase, did not change between the separate period and the interaction period (Figure

258   2C, n=33 trials, 14.1+/-3.4% whisking separate vs 14.4+/-4.3% whisking interaction, and 8.9+/-

259   3.8% forelimb separate vs 9.8+/-4.8% forelimb interaction period, n=33 trials, p=0.77, paired t-

260   test). The total number of behavior events did not differ across trial phases (Supplemental figure

261   1a-b). Behavior periods across mice exhibited temporal coordination, as shown by the peak in

262   the cross-correlation of binary behavior vectors at time lag 0s (Figure 2D black). This temporal

263   relationship was compared with the cross-correlation of the two behavior vectors measured from

264   the stationary mouse during the separate phases of the experiment (Figure 2D, red). The

265   correlation at 0 lag was significantly greater for the inter-animal behaviors compared to the two

266   separate epochs from the stationary mouse (Figure 2d, n=33 trials, 0.32 +/- 0.11 together vs 0.17

267   +/- 0.11 separate, p=6.1×10^{-8}, paired t-test), as well as any other combination of epochs that

268   included at least one separated period (Supplemental figure 1c). Intersection over union for the

269   two behavior vectors (a measure of shared behavior) was significantly greater across animals

270   than across the separate epochs (Figure 2e, n=33 trials, 0.19 +/- 0.09 together vs 0.09+/-0.07

271   separate, p=1×10^{-6}, paired t-test).
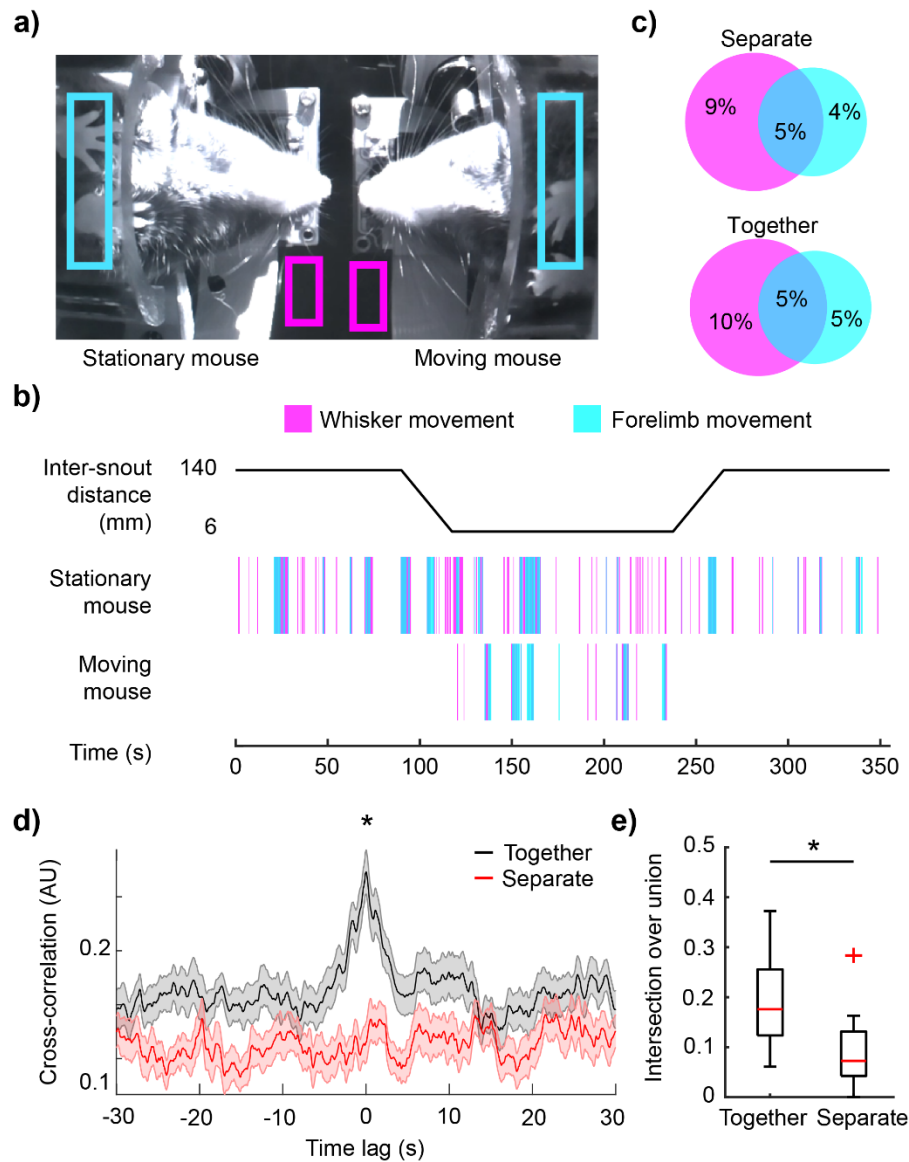
Figure 2. Mice coordinate behavior during interaction. A) Example image of both mice during the interaction phase of the experiment. Regions over each mouse's whiskers and forelimbs are shown in magenta and cyan boxes, respectively, to estimate motion. B) Timeline of experimental paradigm (top) and ethograms for the stationary and moving mouse (bottom). C) Average percentage of time spent behaving during the first separated phase of the experiment (top) and the interaction phase (bottom). Intersecting regions show concurrent whisker and forelimb movements. D) Cross-correlation of each mouse's binary behavior vectors during the interaction phase (black), compared with cross-correlation from the stationary mouse's behavior vectors during the first and second separate phases (red). Behaviors across mice during the interaction phase were significantly correlated near 0 lag. E) Intersection over union for the behavior vectors was significantly greater during the interaction phase across mice than for the behavior vectors of the two separate phases from the stationary mouse. $p<0.05$; t-test.

287   *Global Calcium Signals Synchronize During Interaction*

288   Global signals were calculated as the spatially averaged $\Delta F/F_0$ across the entire masked

289   region of the two cortical hemispheres (Figure 3A-B). Global signal synchronization, measured as

290   the Pearson's correlation coefficient (PCC) between global signals from each mouse, was

291   significantly higher during the interaction phase (0.19 +/- 0.23 interaction phase) of the

292   experiment than during either of the two separate phases (-0.007 +/- 0.13 before; -0.01 +/- 0.14

293   after). (Figure 3C, repeated measures ANOVA, n=35 trials, trial-phase: $F_{2,68} = 11.2$, p = 0.002=).

294   Cagemate vs non-cagemate pairings did not have a significant effect on inter-brain correlation

295   (repeated measures ANOVA, $F_{1,34} = 6x10^{-4}$, p = 0.99). This increase in inter-brain correlation was

296   not observed in experiments using the Thy1-GFP mouse line (Feng et al., 2000), suggesting that

297   hemodynamic contributions to the fluorescence signal do not account for this synchronization

298   (Supplemental Figure 2). Additionally, inter-brain PCCs during the interaction phase were

299   significantly higher than PCCs observed across trial-shuffled global signal pairings during the

300   interaction phase (Figure 3C, 0.02 +/- 0.14, n=35 correct pairs vs n=595 shuffled pairs, $p=1.2x10^{-11}$,

301   t-test), suggesting that inter-brain synchronization is interaction-specific and cannot be

302   attributed to environmental variables shared across trials e.g. timing of the stage translation. An

303   expanded view of the interaction period from Figure 3B is shown with behavior annotations in

304   Figure 3D. Prominent calcium events are often accompanied by sustained periods of behavior

305   (Figure 3D) and the average $\Delta F/F_0$ during the behavior event was positively correlated with

306   behavior duration (Figure 3E, n=2075 behavior events, r=0.44, p<0.001). The time-varying

307   coherence between brains revealed an increase in global signal coherence during the interaction

308   phase at frequencies below 0.2Hz (Figure 3F), suggesting that the large, low-frequency calcium

309   signals observed during behavior periods drive the interbrain global signal synchronization.

310
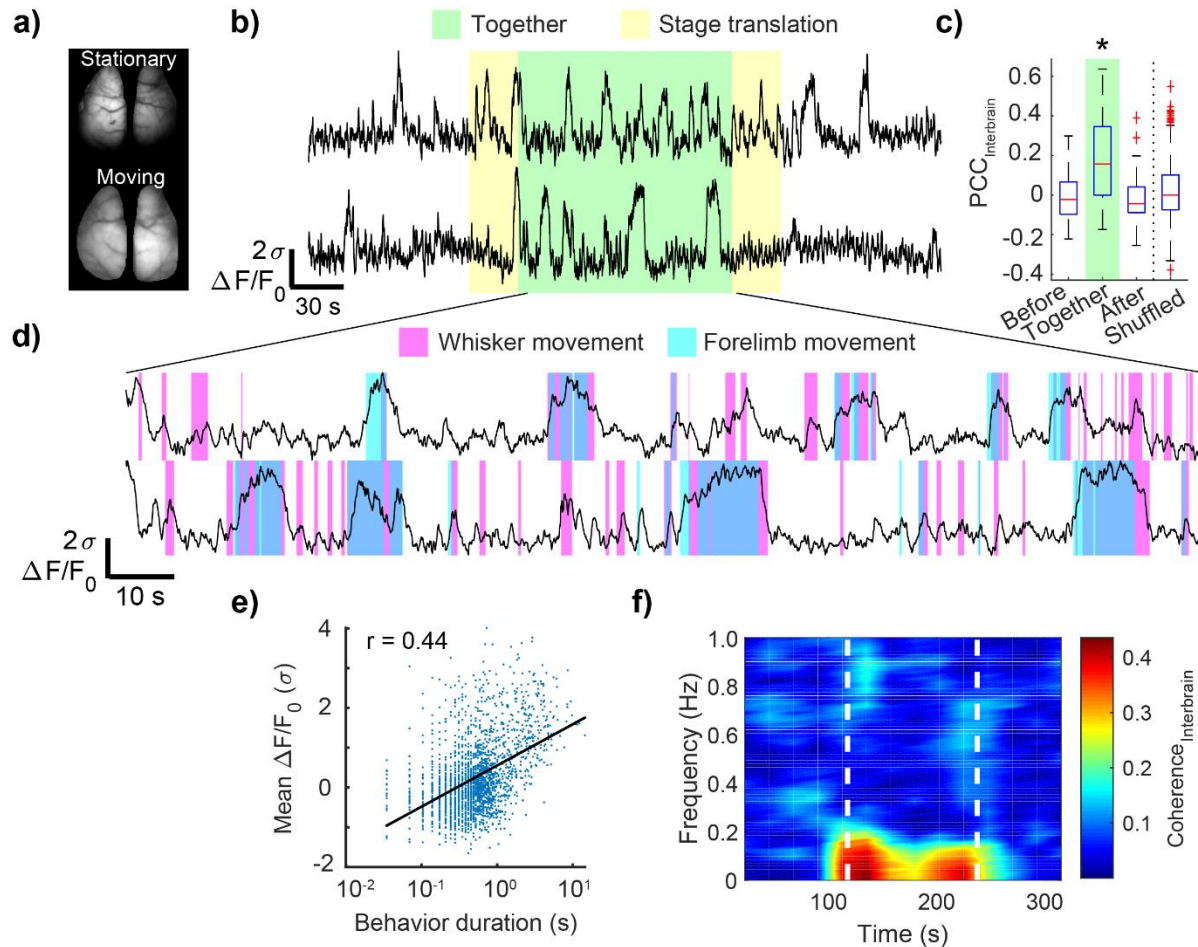
Figure 3. Global signal synchronization during mouse interaction. A) Example images of dorsal cortical windows for each mouse. B) Representative example of GCaMP6s activity averaged across the cortical mask for each mouse. C) Pearson correlation coefficients of the two global signals were significantly greater during the interaction phase than either of the two separate phases (p<0.001; repeated measures ANOVA with post-hoc Bonferroni correction for multiple comparisons). Inter-brain correlations during interaction were significantly greater than trial-shuffled interaction-phase pairings (p<0.001; t-test). D) Expanded view of global signals during interaction phase with behavior annotations overlaid. E) Global signal $\Delta F/F_0$ is positively correlated with duration of behavior (Pearson correlation coefficient; r=0.44; p<0.001). F) Time-varying inter-brain coherence, computed with a 45s window and averaged across all experiments, shows an increase in coherence from 0-0.2Hz during the interaction phase (white dashed lines).

323

324   *Inter-brain synchronization across multiple cortical regions during social interaction*

325   To determine whether the increase in cortex-wide inter-brain synchronization during

326   social interaction was a global phenomenon or instead attributed to specific cortical regions, we

327   examined inter-brain correlations on a region-by-region basis, including motor areas (vibrissae

328   motor cortex, vM1; secondary motor cortex, M2; anterior lateral motor cortex, ALM), sensory

329   areas (primary visual cortex, V1; forelimb, FL; hindlimb, HL, and anterior and posterior barrel

330   cortex, aBC and pBC), retrosplenial, (RS), and parietal association area (PTA) (Figure 4A). All

331   selected regions showed a relative increase in inter-brain correlation during the interaction

332   period (Figure 4B-C, 0.17+/-0.03 together vs -0.013+/-0.009 before and -0.019+/-0.02 after

333   interaction; repeated measures ANOVA, n=35 trials, $F_{2,18}$ = 53.8, p = 8.1x10^{-5},), with the most

334   dramatic increase observed from pBC. Intra-brain correlations also showed a slight but significant

335   increase during the interaction period (Supplemental Figure 3, n=35 trials, p<0.05, repeated

336   measures ANOVA with post-hoc Bonferroni correction).

337   Given the relatively large increase in inter-brain correlation observed from the barrel

338   cortex areas, we wondered if shared sensory experiences during social tactile investigation could

339   underlie the increase in inter-brain correlation. We examined self-initiated and partner-initiated

340   whisking montages, which show cortical dynamics surrounding whisking bout initiation events.

341   Averaged self-initiated and partner-initiated montages showed activation of the posterior barrel

342   cortex area (Figure 4D), confirming that whisking activity elicited by either mouse can elicit barrel

343   cortex responses in both mice (i.e. a shared sensory experience). To test if this shared sensory

344   experience was important for establishing the inter-brain correlation, we performed experiments

345   with physical barriers in place to prevent whisker-whisker contact between mice. Significant

346   increases in region by region inter-brain correlation were not observed when physical contact

347   was prevented using an opaque cardboard sheet or a transparent copper mesh (Figure 4e, open

348   trials: 0.17+/-0.19 together vs -0.007+/-0.11 before and -0.005+/-0.11 after interaction; repeated

349   measures ANOVA, n=35 trials, $F_{2,68}$ = 13.95, p=0.0007; opaque trials: -0.023+/-1.3 together vs -

350   0.024+/-0.09 before and 0.03+/-1.3 after, repeated measures ANOVA, n=15, $F_{2,28}$ = 1.0, p = 0.34;

351   mesh trials: 0.09+/-0.22 together vs -0.011+/-0.11 before and -0.012+/-0.11 after, repeated

352   measures ANOVA n=16, $F_{2,30}$ = 0.022, p = 0.88). Cagemate vs non-cagemate effects were not

353   significant (open trials: $F_{1,34}$ = 3.2x10^{-5}, p = 1.0; opaque trials: $F_{1,13}$ = 0.62, p = 0.45; mesh trials:

354   $F_{1,14}$ = 0.63, p = 0.44). Furthermore, no ultrasonic vocalizations were observed during these

355   experiments (Supplemental Figure 4).

356
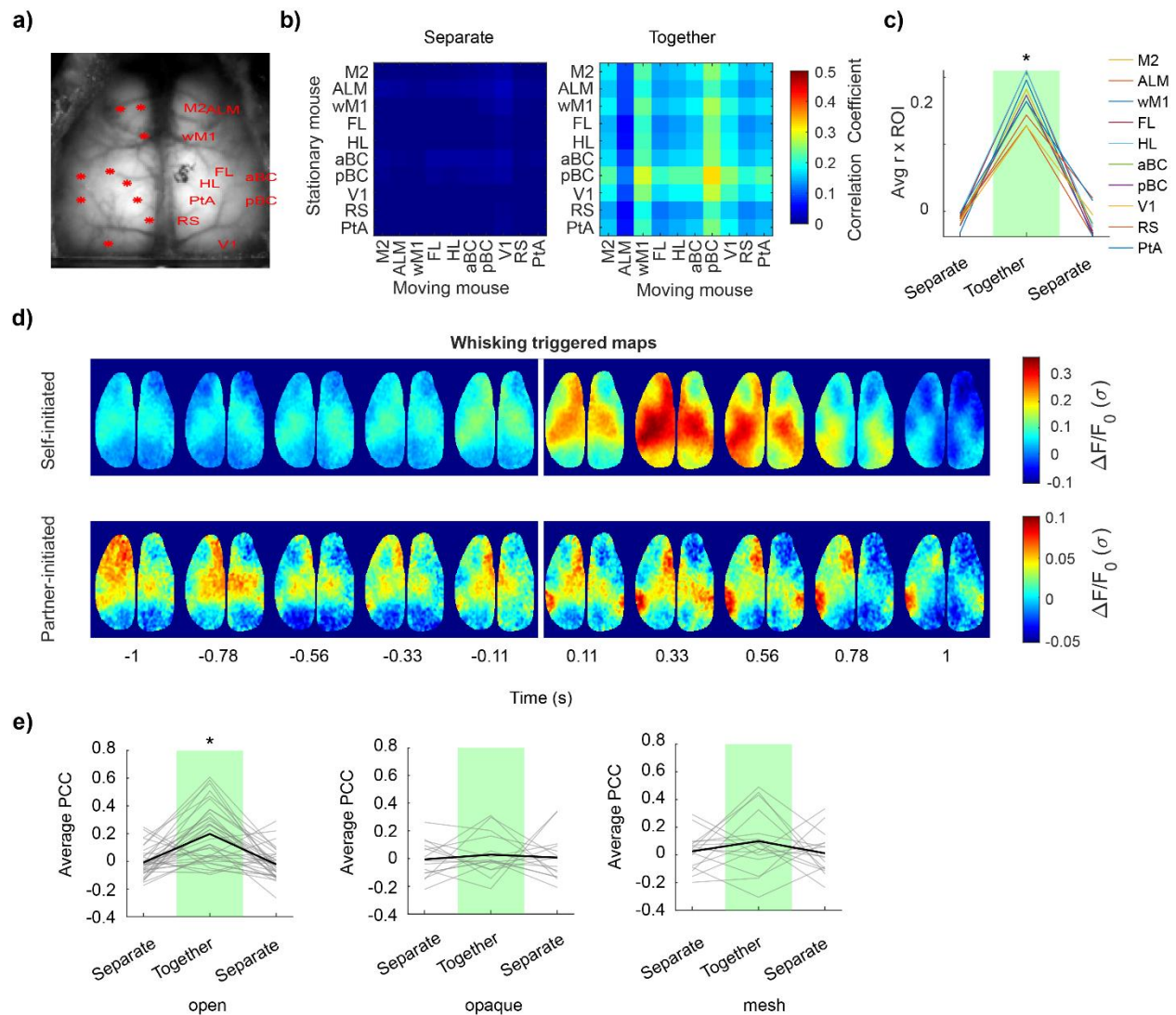
Figure 4. Whisker contact drives multi-region inter-brain synchronization. A) Example image of transcranial mask with regions labelled. Abbreviations: ALM, anterior lateral motor cortex; M2, secondary motor cortex; vM1, vibrissae motor cortex; aBC, anterior barrel cortex; pBC, posterior barrel cortex; HL, hindlimb; FL; forelimb; lPTA; lateral parietal association area; RS, retrosplenial cortex; V1, primary visual cortex. B) Averaged inter-brain correlation matrices across all experiments during the period before interaction (left) and the period during interaction (right). C) Average inter-brain correlation for each region of interest against all other regions, averaged across mice (*$p<0.05$; repeated measures ANOVA with post-hoc Bonferroni correction). Error bars not shown for clarity. D) Example montage showing whisker movement triggered activity. E) Averaged region-by-region correlations in each trial phase for open interaction experiments (left, n=35) and barrier controls (middle, n=15; right, n=16). Individual trials are represented by thin grey lines, and trial averages are represented by thick black lines (*$p<0.001$, repeated measures ANOVA with post-hoc Bonferroni correction).

370

371   *Cortical activation during whisking on familiar partner is stronger than non-familiar partner*

372   To determine if partner identity has an effect on cortical activity, we examined the

373   relationship between social rank and social novelty on cortical dynamics. Social rank differences

374   between cagemate partners, as determined by the tube test assay, were not strongly correlated

375   to the magnitude of global signal inter-brain synchrony at the cortex-wide scale (Figure 5A, n=14

376   trials, Pearson's r=0.15, p=0.6). Similarly, no differences in inter-brain synchronization were seen

377   when comparing interactions between cagemates vs interactions between non-cagemates

378   (Figure 5B, cagemates n=16 trials, 0.18 +/- 0.23; non-cagemates, n=7 trials, 0.21 +/- 0.24; t-test;

379   p=0.66). However, self-initiated whisking events produced greater global cortical activation

380   during cagemate trials compared to non-cagemate trials (Figure 5C-E, cagemates n=40 trials,

381   0.09+/-0.19; non-cagemates, n=26 trials, -0.07+/-0.23; p=0.002, t-test). This difference could not

382   be attributed to differences in the number or duration of whisking bouts (Figure F-G, number of

383   whisking events: 12.1 +/- 4.3 cagemates vs 11.3 +/- 3.4 non-cagemates, p=0.4, t-test; duration of

384   whisking events, 0.27 +/- 0.08 s cagemates vs 0.27 +/- 0.06, p=0.1.0, t-test).
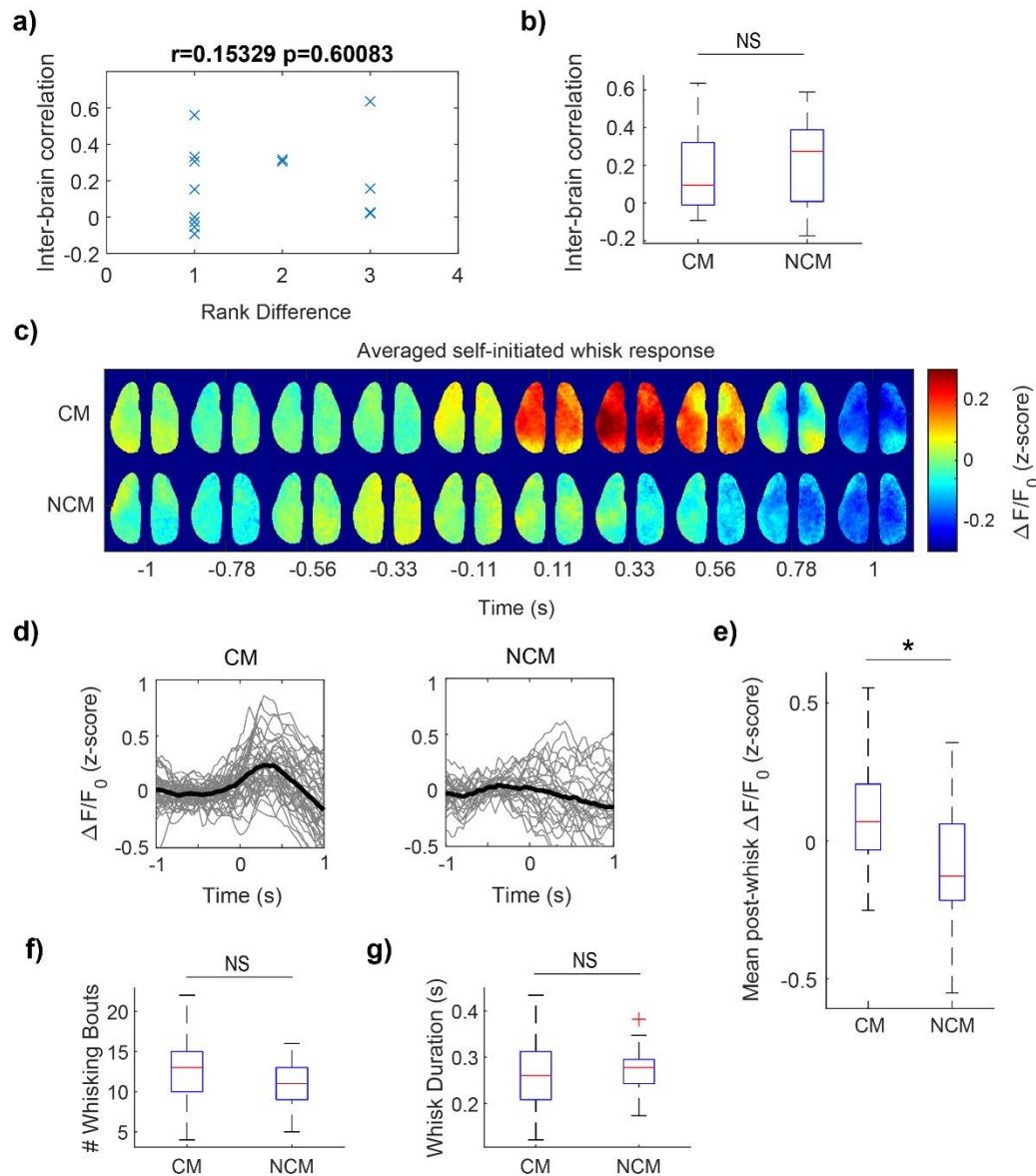
Figure 5. Widespread cortical activation during whisking on a familiar versus novel partner. A) Inter-brain global signal correlation is not related to social rank differences between interacting partners (Pearson correlation coefficient, r=0.15). B) Inter-brain signal correlation does not depend on cagemate vs non-cagemate experiments (t-test, p=0.66). C) Self-initiated whisk event triggered activation maps for cagemates and non-cagemates, averaged across all whisk events per mouse then averaged across mice. D) Global signals associated with whisk-triggered events for cagemates and non-cagemates. Thin gray lines show averaged global signals across all whisking events per mouse. Thick black lines show average across mice. E) The mean $\Delta F/F_0$ in the 1-s post-whisk period was significantly greater in the cagemate group compared to the non-cagemate group (t-test, p=0.005). F-G) Number of whisking bouts and duration of whisking bouts were not different between cagemate and non-cagemate groups.

Discussion

Our results indicate widespread correlated cortical activity between the brains of interacting mice. This synchrony is not associated with the mechanics or timing of the imaging paradigm as it was not present when trial-shuffled mouse pairs were examined. Rather, the inter-animal cortical synchronization is likely driven by temporally coordinated bouts of behavior (e.g. whisking or forelimb movements) and shared somatosensory experiences. Although previous work found that the magnitude of inter-brain synchronization may convey information regarding the social status of one of the individuals (Jiang et al., 2015; Kingsbury et al., 2019), we did not find a relationship between social rank differences and cortex-wide inter-brain synchronization. Surprisingly, we found that whisking behavior in the presence of a familiar conspecific partner elicited more pronounced cortical activation compared to whisking onto a non-familiar partner. This difference may suggest a macroscale cortical network representation of social partner identity. Future work will examine the contribution of social sensory cues on cortex-wide behavior and individual sensory circuits.

One limitation of the presented work is that the frame rate of the behavior camera was not fast enough to clearly resolve whisker movements. Detailed analyses of whisker movements in mice typically use camera acquisition rates of ~500fps (Mayrhofer et al., 2019; Sofroniew, Cohen, Lee, & Svoboda, 2014). It is possible that some whisking events were missed by our analyses, or the precise timing of whisk initiation was not accurately resolved. Nevertheless, whisker motion energy measurements resolved the initiation of gross whisking events, as suggested by the cortical maps displaying barrel and vibrissae motor cortex activation (Figure

419 4d); and false-negative error rates should presumably be consistent across experiments. Another

420 limitation of the presented work is that mice must be head-restrained in order to be imaged and

421 positioned properly. In a previous study, head-fixation was found to be aversive, but with training

422 and habituation stress recedes (Z. V Guo et al., 2014) and rodents can even be trained to restrain

423 themselves (Aoki, Tsubota, Goya, & Benucci, 2017; Murphy et al., 2020; Scott, Brody, & Tank,

424 2013). For this reason, we present the results as an interaction that occurs in the context of head-

425 fixation and caution that the observed brain dynamics may not reflect true naturalistic social

426 touch behavior. Despite this, head-restraint facilitates consistent and reproducible interactions

427 between animals, allowing for trial-averaging of behaviors. Recent development of a head-

428 mounted mesoscopic camera allows for the exciting possibility to examine cortex-wide neural

429 dynamics during more naturalistic social interactions in freely-moving mice (Rynes et al., 2020).

430   In conclusion, we introduce a dual mouse mesoscale imaging platform that can create

431 reproducible interactions between mice that constrains some of the possible behaviors and

432 timing due to the head-restrained and rail-based system. Such a constraint may be particularly

433 important when evaluating the behavior of different mouse mutants associated with disorder of

434 social interactions, such as the SHANK3 mutant mice (Peça et al., 2011). Future experiments can

435 incorporate simultaneous electrophysiological recordings (Xiao et al., 2017) or examine lower

436 frequency events that are revealed using functional near-infrared spectroscopy or intrinsic

437 optical signals to draw parallels to human studies analyzing inter-subject interactions.

438

439 **References**

440 Allen, W. E., Chen, M. Z., Pichamoorthy, N., Tien, R. H., Pachitariu, M., Luo, L., & Deisseroth, K. (2019).

441   Thirst regulates motivated behavior through modulation of brainwide neural population dynamics.
442   *Science*, *364*(6437), 253. https://doi.org/10.1126/science.aav3932

443   Allen, W. E., Kauvar, I. V, Chen, M. Z., Richman, E. B., Yang, S. J., Chan, K., … Deisseroth, K. (2017). Global
444   Representations of Goal-Directed Behavior in Distinct Cell Types of Mouse Neocortex. *Neuron*,
445   *94*(4), 891-907.e6. https://doi.org/10.1016/j.neuron.2017.04.017

446   Aoki, R., Tsubota, T., Goya, Y., & Benucci, A. (2017). An automated platform for high-throughput mouse
447   behavior and physiology with voluntary head-fixation. *Nature Communications*.
448   https://doi.org/10.1038/s41467-017-01371-0

449   Bobrov, E., Wolfe, J., Rao, R. P., & Brecht, M. (2014). The representation of social facial touch in rat
450   barrel cortex. *Current Biology*. https://doi.org/10.1016/j.cub.2013.11.049

451   Bokil, H., Andrews, P., Kulkarni, J. E., Mehta, S., & Mitra, P. P. (2010). Chronux: A platform for analyzing
452   neural signals. *Journal of Neuroscience Methods*. https://doi.org/10.1016/j.jneumeth.2010.06.020

453   Chen, P., & Hong, W. (2018). Neural Circuit Mechanisms of Social Behavior. *Neuron*.
454   https://doi.org/10.1016/j.neuron.2018.02.026

455   Chen, T.-W., Wardill, T. J., Sun, Y., Pulver, S. R., Renninger, S. L., Baohan, A., … Kim, D. S. (2013).
456   Ultrasensitive fluorescent proteins for imaging neuronal activity. *Nature*, *499*(7458), 295–300.
457   https://doi.org/10.1038/nature12354

458   Clancy, K. B., Orsolic, I., & Mrsic-Flogel, T. D. (2019). Locomotion-dependent remapping of distributed
459   cortical networks. *Nat. Neurosci.*, *22*(5), 778–786. https://doi.org/10.1038/s41593-019-0357-8

460   Coffey, K. R., Marx, R. G., & Neumaier, J. F. (2019). DeepSqueak: a deep learning-based system for
461   detection and analysis of ultrasonic vocalizations. *Neuropsychopharmacology*.
462   https://doi.org/10.1038/s41386-018-0303-6

463   Cohen, L., Rothschild, G., & Mizrahi, A. (2011). Multisensory integration of natural odors and sounds in
464   the auditory cortex. *Neuron*. https://doi.org/10.1016/j.neuron.2011.08.019

465   Dana, H., Chen, T.-W., Hu, A., Shields, B. C., Guo, C., Looger, L. L., … Svoboda, K. (2014). Thy1-GCaMP6
466   Transgenic Mice for Neuronal Population Imaging In Vivo. *PLoS One*, *9*(9), e108697.
467   https://doi.org/10.1371/journal.pone.0108697

468   Dikker, S., Wan, L., Davidesco, I., Kaggen, L., Oostrik, M., McClintock, J., … Poeppel, D. (2017). Brain-to-
469   Brain Synchrony Tracks Real-World Dynamic Group Interactions in the Classroom. *Current Biology*.
470   https://doi.org/10.1016/j.cub.2017.04.002

471   Dölen, G., Darvishzadeh, A., Huang, K. W., & Malenka, R. C. (2013). Social reward requires coordinated
472   activity of nucleus accumbens oxytocin and serotonin. *Nature*.
473   https://doi.org/10.1038/nature12518

474   Ebbesen, C. L., Bobrov, E., Rao, R. P., & Brecht, M. (2019). Highly structured, partner-sex- and subject-
475   sex-dependent cortical responses during social facial touch. *Nature Communications*.
476   https://doi.org/10.1038/s41467-019-12511-z

477   Fan, Z., Zhu, H., Zhou, T., Wang, S., Wu, Y., & Hu, H. (2019). Using the tube test to measure social
478   hierarchy in mice. *Nat. Protoc.*, *14*(3), 819–831. https://doi.org/10.1038/s41596-018-0116-4

479   Feng, G., Mellor, R. H., Bernstein, M., Keller-Peck, C., Nguyen, Q. T., Wallace, M., … Sanes, J. R. (2000).

480   Imaging neuronal subsets in transgenic mice expressing multiple spectral variants of GFP. *Neuron*,
481   *28*(1), 41–51. Retrieved from https://www.ncbi.nlm.nih.gov/pubmed/11086982

482   Funane, T., Kiguchi, M., Atsumori, H., Sato, H., Kubota, K., & Koizumi, H. (2011). Synchronous activity of
483   two people's prefrontal cortices during a cooperative task measured by simultaneous near-infrared
484   spectroscopy. *J. Biomed. Opt.*, *16*(7), 77011. https://doi.org/10.1117/1.3602853

485   Gilad, A., & Helmchen, F. (2020). Spatiotemporal refinement of signal flow through association cortex
486   during learning. *Nat. Commun.*, *11*(1), 1744. https://doi.org/10.1038/s41467-020-15534-z

487   Gunaydin, L. A., Grosenick, L., Finkelstein, J. C., Kauvar, I. V., Fenno, L. E., Adhikari, A., … Deisseroth, K.
488   (2014). Natural neural projection dynamics underlying social behavior. *Cell*.
489   https://doi.org/10.1016/j.cell.2014.05.017

490   Guo, B., Chen, J., Chen, Q., Ren, K., Feng, D., Mao, H., … Wu, S. (2019). Anterior cingulate cortex
491   dysfunction underlies social deficits in Shank3 mutant mice. *Nat. Neurosci.*, *22*(8), 1223–1234.
492   https://doi.org/10.1038/s41593-019-0445-9

493   Guo, Z. V, Li, N., Huber, D., Ophir, E., Gutnisky, D., Ting, J. T., … Svoboda, K. (2014). Flow of cortical
494   activity underlying a tactile decision in mice. *Neuron*, *81*(1), 179–194.
495   https://doi.org/10.1016/j.neuron.2013.10.020

496   Jiang, J., Chen, C., Dai, B., Shi, G., Ding, G., Liu, L., & Lu, C. (2015). Leader emergence through
497   interpersonal neural synchronization. *Proceedings of the National Academy of Sciences*.
498   https://doi.org/10.1073/pnas.1422930112

499   Kingsbury, L., Huang, S., Raam, T., Ye, L. S., Wei, D., Hu, R. K., … Hong, W. (2020). Cortical
500   Representations of Conspecific Sex Shape Social Behavior. *Neuron*.
501   https://doi.org/10.1016/j.neuron.2020.06.020

502   Kingsbury, L., Huang, S., Wang, J., Gu, K., Golshani, P., Wu, Y. E., & Hong, W. (2019). Correlated Neural
503   Activity and Encoding of Behavior across Brains of Socially Interacting Animals. *Cell*.
504   https://doi.org/10.1016/j.cell.2019.05.022

505   Kluyver, T., Ragan-Kelley, B., Pérez, F., Granger, B. E., Bussonnier, M., Frederic, J., … Others. (2016).
506   Jupyter Notebooks-a publishing format for reproducible computational workflows. *ELPUB*.
507   Retrieved from
508   https://books.google.com/books?hl=en&lr=&id=Lgy3DAAAQBAJ&oi=fnd&pg=PA87&dq=kluyver+2
509   016+Jupyter&ots=N1AX7LqGbm&sig=_iRTlQYM8bahTMPNiqSV-dE9JkE

510   Lenschow, C., & Brecht, M. (2015). Barrel Cortex Membrane Potential Dynamics in Social Touch. *Neuron*.
511   https://doi.org/10.1016/j.neuron.2014.12.059

512   Li, Y., Mathis, A., Grewe, B. F., Osterhout, J. A., Ahanonu, B., Schnitzer, M. J., … Dulac, C. (2017).
513   Neuronal Representation of Social Information in the Medial Amygdala of Awake Behaving Mice.
514   *Cell*. https://doi.org/10.1016/j.cell.2017.10.015

515   Liu, Y., Piazza, E. A., Simony, E., Shewokis, P. A., Onaral, B., Hasson, U., & Ayaz, H. (2017). Measuring
516   speaker-listener neural coupling with functional near infrared spectroscopy. *Sci. Rep.*, *7*, 43293.
517   https://doi.org/10.1038/srep43293

518   Ma, Y., Shaik, M. A., Kim, S. H., Kozberg, M. G., Thibodeaux, D. N., Zhao, H. T., … Hillman, E. M. C. (2016).
519   Wide-field optical mapping of neural activity and brain haemodynamics: considerations and novel

520   approaches. *Philos. Trans. R. Soc. Lond. B Biol. Sci.*, *371*(1705).
521   https://doi.org/10.1098/rstb.2015.0360

522 MacDowell, C. J., & Buschman, T. J. (2020). Low-Dimensional Spatiotemporal Dynamics Underlie Cortex-
523   wide Neural Activity. *Current Biology*. https://doi.org/10.1016/j.cub.2020.04.090

524 Mayrhofer, J. M., El-Boustani, S., Foustoukos, G., Auffret, M., Tamura, K., & Petersen, C. C. H. (2019).
525   Distinct Contributions of Whisker Sensory Cortex and Tongue-Jaw Motor Cortex in a Goal-Directed
526   Sensorimotor Transformation. *Neuron*, *103*(6), 1034-1043.e5.
527   https://doi.org/10.1016/j.neuron.2019.07.008

528 Mitra, P., & Bokil, H. (2009). *Observed Brain Dynamics*. *Observed Brain Dynamics*.
529   https://doi.org/10.1093/acprof:oso/9780195178081.001.0001

530 Montague, P. R., Berns, G. S., Cohen, J. D., McClure, S. M., Pagnoni, G., Dhamala, M., … Fisher, R. E.
531   (2002). Hyperscanning: simultaneous fMRI during linked social interactions. *Neuroimage*, *16*(4),
532   1159–1164. https://doi.org/10.1006/nimg.2002.1150

533 Murphy, T. H., Michelson, N. J., Boyd, J. D., Fong, T., Bolaños, L. A., Bierbrauer, D., … Ledue, J. M. (2020).
534   Automated task training and longitudinal monitoring of mouse mesoscale cortical circuits using
535   home cages. *ELife*. https://doi.org/10.7554/eLife.55964

536 Musall, S., Kaufman, M. T., Juavinett, A. L., Gluf, S., & Churchland, A. K. (2019). Single-trial neural
537   dynamics are dominated by richly varied movements. *Nature Neuroscience*.
538   https://doi.org/10.1038/s41593-019-0502-4

539 Peça, J., Feliciano, C., Ting, J. T., Wang, W., Wells, M. F., Venkatraman, T. N., … Feng, G. (2011). Shank3
540   mutant mice display autistic-like behaviours and striatal dysfunction. *Nature*, *472*(7344), 437–442.
541   https://doi.org/10.1038/nature09965

542 Pinto, L., Rajan, K., DePasquale, B., Thiberge, S. Y., Tank, D. W., & Brody, C. D. (2019). Task-Dependent
543   Changes in the Large-Scale Dynamics and Necessity of Cortical Regions. *Neuron*.
544   https://doi.org/10.1016/j.neuron.2019.08.025

545 Rogers-Carter, M. M., Varela, J. A., Gribbons, K. B., Pierce, A. F., McGoey, M. T., Ritchey, M., &
546   Christianson, J. P. (2018). Insular cortex mediates approach and avoidance responses to social
547   affective stimuli. *Nature Neuroscience*. https://doi.org/10.1038/s41593-018-0071-y

548 Rynes, M., Surinach, D., Laroque, M., Linn, S., Dominguez, J., Ghanbari, L., & Kodandaramaiah, S. (2020).
549   Miniaturized device for whole cortex mesoscale imaging in freely behaving mice. *Neural Imaging*
550   *and Sensing 2020*. https://doi.org/10.1117/12.2550395

551 Scott, B. B., Brody, C. D., & Tank, D. W. (2013). Cellular resolution functional imaging in behaving rats
552   using voluntary head restraint. *Neuron*, *80*(2), 371–384.
553   https://doi.org/10.1016/j.neuron.2013.08.002

554 Silasi, G., Xiao, D., Vanni, M. P., Chen, A. C. N., & Murphy, T. H. (2016). Intact skull chronic windows for
555   mesoscopic wide-field imaging in awake mice. *Journal of Neuroscience Methods*.
556   https://doi.org/10.1016/j.jneumeth.2016.04.012

557 Sofroniew, N. J., Cohen, J. D., Lee, A. K., & Svoboda, K. (2014). Natural whisker-guided behavior by head-
558   fixed mice in tactile virtual reality. *Journal of Neuroscience*, *34*(29), 9537–9550. Retrieved from
559   https://www.jneurosci.org/content/34/29/9537/

560 Steinmetz, N. A., Zatka-Haas, P., Carandini, M., & Harris, K. D. (2019). Distributed coding of choice, action
561   and engagement across the mouse brain. *Nature*, *576*(7786), 266–273.
562   https://doi.org/10.1038/s41586-019-1787-x

563 Sych, Y., Chernysheva, M., Sumanovski, L. T., & Helmchen, F. (n.d.). High-density multi-fiber photometry
564   for studying large-scale brain circuit dynamics. https://doi.org/10.1101/422857

565 Tschida, K., Michael, V., Takatoh, J., Han, B.-X., Zhao, S., Sakurai, K., … Wang, F. (2019). A Specialized
566   Neural Circuit Gates Social Vocalizations in the Mouse. *Neuron*, *103*(3), 459-472.e4.
567   https://doi.org/10.1016/j.neuron.2019.05.025

568 Valley, M. T., Moore, M. G., Zhuang, J., Mesa, N., Castelli, D., Sullivan, D., … Waters, J. (2020). Separation
569   of hemodynamic signals from GCaMP fluorescence measured with wide-field imaging. *Journal of*
570   *Neurophysiology*. https://doi.org/10.1152/JN.00304.2019

571 Vanni, M. P., Chan, A. W., Balbi, M., Silasi, G., & Murphy, T. H. (2017). Mesoscale Mapping of Mouse
572   Cortex Reveals Frequency-Dependent Cycling between Distinct Macroscale Functional Modules. *J.*
573   *Neurosci.*, *37*(31), 7513–7533. https://doi.org/10.1523/jneurosci.3560-16.2017

574 Vanni, M. P., & Murphy, T. H. (2014). Mesoscale transcranial spontaneous activity mapping in GCaMP3
575   transgenic mice reveals extensive reciprocal connections between areas of somatomotor cortex. *J.*
576   *Neurosci.*, *34*(48), 15931–15946. https://doi.org/10.1523/JNEUROSCI.1818-14.2014

577 Walsh, J. J., Christoffel, D. J., Heifets, B. D., Ben-Dor, G. A., Selimbeyoglu, A., Hung, L. W., … Malenka, R.
578   C. (2018). 5-HT release in nucleus accumbens rescues social deficits in mouse autism model.
579   *Nature*. https://doi.org/10.1038/s41586-018-0416-4

580 Wang, F., Zhu, J., Zhu, H., Zhang, Q., Lin, Z., & Hu, H. (2011). Bidirectional control of social hierarchy by
581   synaptic efficacy in medial prefrontal cortex. *Science*. https://doi.org/10.1126/science.1209951

582 Wekselblatt, J. B., Flister, E. D., Piscopo, D. M., & Niell, C. M. (2016). Large-scale imaging of cortical
583   dynamics during sensory perception and behavior. *Journal of Neurophysiology*.
584   https://doi.org/10.1152/jn.01056.2015

585 Xiao, D., Vanni, M. P., Mitelut, C. C., Chan, A. W., Ledue, J. M., Xie, Y., … Murphy, T. H. (2017). Mapping
586   cortical mesoscopic networks of single spiking cortical or sub-cortical neurons. *ELife*.
587   https://doi.org/10.7554/eLife.19976

588 Yang, J., Zhang, H., Ni, J., De Dreu, C. K. W., & Ma, Y. (2020). Within-group synchronization in the
589   prefrontal cortex associates with intergroup conflict. *Nature Neuroscience*.
590   https://doi.org/10.1038/s41593-020-0630-x

591 Zhang, W., & Yartsev, M. M. (2019). Correlated Neural Activity across the Brains of Socially Interacting
592   Bats. *Cell*. https://doi.org/10.1016/j.cell.2019.05.023

593 Zhou, T., Zhu, H., Fan, Z., Wang, F., Chen, Y., Liang, H., … Hu, H. (2017). History of winning remodels
594   thalamo-PFC circuit to reinforce social dominance. *Science*, *357*(6347), 162–168.
595   https://doi.org/10.1126/science.aak9726

596

597

Table 1: Parts List for Social Interaction System

Description	#	Manufacturer	Part Number
Aluminum Breadboard 18" x 24" x 1/2", 1/4"-20 Taps	1	Thorlabs	MB1824
Ø1" Pillar Posts with 1/4"-20 Taps, 2"	4	Thorlabs	RS2
Ø1" Pillar Posts with 1/4"-20 Taps, 3"	8	Thorlabs	RS3
Ø1" Pillar Posts with 1/4"-20 Taps, 6"	8	Thorlabs	RS6
Clamping Fork, 1.24" Counterbored Slot, Universal	4	Thorlabs	CF125
Ø1/2" Pedestal Post Holder	3	Thorlabs	PH2E
Ø1/2" Optical Post, SS, 8-32 Setscrew, 1/4"-20 Tap, L = 8"	3	Thorlabs	TR8
Ø1/2" Optical Post, SS, 8-32 Setscrew, 1/4"-20 Tap, L = 12"	1	Thorlabs	TR12
Right-Angle Clamp for Ø1/2" Posts, 3/16" Hex	2	Thorlabs	RA90
Ø25 mm Post Spacer, Thickness = 3 mm	1	Thorlabs	RS3M
RPi Camera (F), Supports Night Vision, Adjustable-Focus	2	Waveshare	10299
Flex Cable for Raspberry Pi Camera or Display - 2 meters	2	Adafruit	2144
Triple Light Guide and Imaging Parts			
Triple Bandpass Filter (camera)	1	Chroma	69013m
Liquid Light Guide	1	Thorlabs	LLG0338-4
SM1 Adapter for Liquid Light Guide	1	Thorlabs	AD3LLG
SM1 Lens Tube, 3.00" Thread Depth	3	Thorlabs	SM1L30
SM1 Lens Tube, 1.00" Thread Depth	3	Thorlabs	SM1L10
SM1 Lens Tube, 2.00" Thread Depth	1	Thorlabs	SM1L20
SM1 Retaining Rings	2	Thorlabs	SM1RR-P10
Dichroic Cage Cube	2	Thorlabs	CM1-DC
Cage Cube Connector	1	Thorlabs	CM1-CC
Compact Clamp with Variable Height	1	Thorlabs	CL3
Bi-Convex Lens	4	Thorlabs	LB1761
AT455DC Size: 26 * 38 mm	1	Chroma	AT455DC
25 mm x 36 mm Longpass Dichroic Mirror, 550 nm Cutoff	1	Thorlabs	DMLP550R
Ø1" Bandpass Filter, CWL = 620 ± 2 nm, FWHM = 10 ± 2 nm	1	Thorlabs	FB620-10
ET480/30x Size: 25mmR R=Mounted in Ring	1	Chroma	ET480/30x

Ø1" Bandpass Filter, CWL = 440 ± 2 nm, FWHM = 10 ± 2 nm	1	Thorlabs	FB440-10
Royal-Blue (448nm) Rebel LED	1	Luxeon Star	SP-01-V4
Blue (470nm) Rebel LED	1	Luxeon Star	SP-01-B6
Red-Orange (617nm) Rebel LED	1	Luxeon Star	SP-01-E6

Machined Parts (Stainless Steel)

Milled as-1.50_2_v2.SLDPRT	3
Spacer_with_wire_hole_as-.500_v2.SLDPRT	3
LED_mount_as-1.50_v2.SLDPRT	3

3D Printed Parts (Black PLA)

TripleLEDLightGuide_Base.stl	1
Light_Guide_Mount_V2.stl	1

598